Textile Based Capacitive Sensor for Physical Rehabilitation *via* Surface Topological Modification

Liming Chen[a], Mingyang Lu[a], Haosen Yang[c], Jorge Ricardo Salas Avila[a], Bowen Shi[b], Lei Ren[c], Guowu Wei[d], Xuqing Liu[b,*], Wuliang Yin[a,*]

[a] Department of Electrical and Electronic Engineering, University of Manchester, Sackville Street Building, Manchester M13 9PL, United Kingdom.

[b] Department of Materials, University of Manchester, Sackville Street Building, Manchester M13 9PL, United Kingdom.

[c] Department of Mechanical, Aerospace and Civil Engineering, University of Manchester, Sackville Street Building, Manchester M13 9PL, United Kingdom.

[d] School of Computing, Science and Engineering, University of Salford, Salford, M5 4WT, United Kingdom.

*E-mail: xuqing.liu@manchester.ac.uk; wuliang.yin@manchester.ac.uk

ABSTRACT: Wearable sensor technologies, especially continuous monitoring of various human health conditions, are attracting increasing attention. However, current rigid sensors present obvious drawbacks, like lower durability and poor comfort. Here, a strategy is proposed to efficiently yield wearable sensors using cotton fabric as an essential component, and conductive materials conformally coat onto the cotton fibers, leading to a highly electrically conductive interconnecting network. To improve the conductivity and durability of conductive coatings, a topographical modification approach is developed with genus-3 and genus-5 structures, and topological genus structures enable cage metallic-seeds on the surface of substrates. A textile-based capacitive sensor with flexible, comfortable, and durable properties has been demonstrated. High sensitivity and convenience of signal collection have been achieved by the excellent electrical conductivity of this sensor. Based on results of deep investigation on capacitance, effects of distance and angles between two conductive fabrics contribute to the capacitive sensitivity. In addition, the textile-based capacitive sensor has successfully been used for real-time monitoring human breathing, speaking, blinking and joint motions during physical rehabilitation exercises.

KEYWORDS: *topological adhesion, nickel nanoparticles, electroless deposition, capacitance sensor, real-time monitoring*

Comfortable and lightweight characters enable textile-based electronic devices to be used in a wider range of applications, compared to conventional heavy and cumbersome electronic devices.[1-4] Particularly, this kind of electronic devices can be simply integrated into wearable formats (*e.g.* clothing) and then provide real-time health monitoring continuously instead of expensive large equipment in a hospital or health center. In fact, as the global population ages, a growing number of elders are suffering from chronic health problems and declining functionality, which poses intensive stress on the healthcare system.[5] This textile-based wearable sensor can collect individual dynamic health signals to diagnose health conditions, which effectively release the burden of hospitalization.

There are various flexible and stretchable electrodes, made from carbon materials, conductive polymers and metal-based electronics, which could be used as conductive materials.[2, 6, 7] Carbon materials, including carbon nanotube (CNT) and graphene, have been used as flexible electronics with reliable and stable properties. Our previous works, taken as an example, have shown graphene coating on the surface of polyurethane (PU) fibers to realize real-time wearable sensation.[8, 9] However, complicated processing, cytotoxicity, and the high-cost have limited the mass-production and practical applications. Conductive polymers, such as poly(3,4-ethylenedioxythiophene):poly(styrenesulfonate) (PEDOT:PSS) and polypyrrole (PPy), have gradually attracted attention due to their excellent flexible properties, while limitations in processing, stability and conductivity have still prevented the widespread use.[2, 10, 11] Metals (*e.g.* silver, aluminum, nickel and copper), as the most common conductive material, exhibit excellent ductility and outstanding conductivity. Nevertheless, the bulk metals are rigid, which limits the application in wearable electronics. When the metal coating is reduced to the micrometer/nanometer scale, it performances excellent flexibility and can be combined with fibers to form a flexible conductive fabric or electrode,[12-14] which dominates the majority of market. However, due to the lack of interaction between substrates and metal

coatings, the durability of the commercialized conductive fabrics and electrodes should be improved.

Until now, several efforts have developed to fabricate textile-based electronic devices, such as atomic layer deposition,[15] physical vapor deposition,[16] electrodeposition,[17] chemical solution process,[12] and polymer-assisted metal deposition (PAMD).[18-21] PAMD consists of three steps (**Figure S1A**), polymer grafting, catalyst loading into polymer network and electroless deposition (ELD) of metal nanoparticles.[22] It has received the most attention contributed by manufacturing conductive textiles in a user-friendly and money-saving way. Unfortunately, some drawbacks still exist in the conventional PAMD process.[23] Toxic solvent like toluene is frequently used in surface-initiated radical polymerization, which is undesirable in wearable textiles.[24, 25] Traditional surface-initiated radical polymerization offers low yields and requires nitrogen protection usually. Very recently, dopamine[14, 20] and tannic acid[18] were introduced to the surface-grafted polymer layer, which is environment-friendly and mass-producible. However, the process of oxypolymerization is time-consuming and difficult to control. The weak hydrogen bonds between the substrate and the surface-grafted linear polymer (**Figure 1A**) may cause the polymer in some regions to fall off. Thus, a controllable chemical reaction process with robust interaction bonds is highly desired.

Herein, the ‘das Geschlecht (genus)’ of the surface from mathematic is proposed to develop a universal strategy in surface modification, and to understand the relationship of surface topology and performances. Mathematician Riemann studied the topology of surfaces, and Clebsch considered surfaces from a more algebraic geometric viewpoint, called p ‘das Geschlecht (genus)’ of the surface to show invariant determines the surface.[26] In traditional materials surface modification, there are no any topographical interactions between coatings and substrates (genus-0, **Figure 1A**). In this work, a topographical modification is developed to improve the surface adhesion force of coating. Genus-3 (**Figure 1B**) and genus-5 surface (**Figure 1C**), inspired by common synthesis method of hydrogel structure, were introduced by

topographical modification of crosslinked polymers (**Figure 1C**). Catalyst-based nickel seed crystals are caged by the genus-3 and genus-5 structures (**Figure 1D and 1F**), to upsurge the density of seed crystals on the surface of modified substrates, and to increase the conductivity in the following deposition process.[27-29] Benefitted from topological adhesion, the robust chemical network enables the subsequent electroless deposited nickel nanoparticles to coat onto the cotton fabric. The obtained conductive fabric can act as a capacitive sensor with high sensitivity. We used the capacitive sensor to investigate the fundamental properties of capacitance change level monitoring. As a proof of concept, it was applied for real-time monitoring of individual respiration, speaking and joint motions during physical rehabilitation exercises.

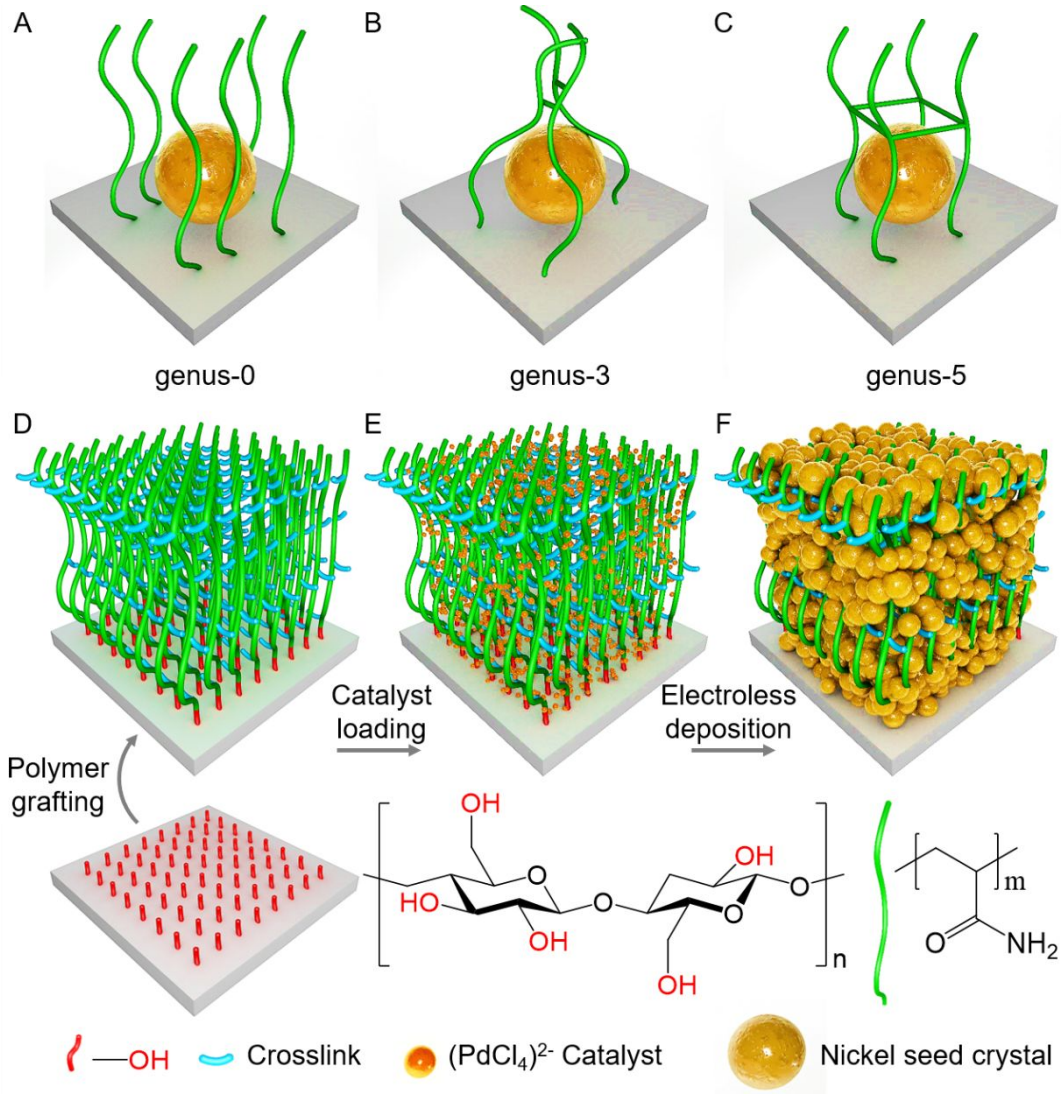

Figure 1. Genus-0 (A), genus-3 (B) and genus-5 (C) surface to cage catalyst-based nickel seed crystal, and schematic illustration of the PAMD fabrication *via* surface nanotechnology,

involved three steps (D) topologies entangled grafting of polymer networks across the gaps and surfaces of cotton fibers, (E) immobilization of catalysts in the polymer networks, (F) and subsequent ELD of nickel nanoparticles at the catalytic active sites to form a nickel nanoparticle film on the surface of cotton fibers.

RESULTS AND DISCUSSION

The microscopic morphologies of fabric composites were characterized by scanning electron microscopy (SEM). AAm uniformly crosslinking with the cotton surface was supported by no obvious morphology difference between the pristine cotton fabric and AAm-crosslinking fabric (**Figure 2A and 2B).** Nickel nanoparticles densely aggregate on the fabric surface (**Figure 2C**). Genus is used to describe an orientable surface, which can be defined in terms of the Euler characteristic χ, *via* the relationship $\chi = 2 - 2g$ for closed surfaces. It is clear in **Figure 2A**, the surface grafted polymer brushes are no inter-connection between each other, so that the genus number of the closed surface is 0. And in **Figure 2B** and **2C**, the linked caged structures is developed, which can capture catalysts and metallic seeds *via* several closed surfaces, according to genus 3 and 5. The closed surfaces formed cage could tether more catalysts and metallic seeds on the surface of substrates, leading to a higher density of metallic deposition, as well as higher conductivity.

The as-prepared nickel-coated conductive fabric was protected using PDMS to prevent nickel particles from falling off (**Figure 2D**). **Figure 2E and 2F** representative SEM images of as-prepared nickel-coated woven and knitted fabrics with an approximate diameter yarn of about 200μm. Every yarn contains many fibers. The enlarged regions of fibers in **Figure 2G** suggested that the uniform and dense nickel nanoparticles (100 nm) self-assemble into a continuously conductive film and aggregate on every fiber unit of the fabric composites. Importantly, the densely structured nickel nano-spheres consisting of many very fine small nanoparticles (10 nm) were formed. This area was further analyzed by EDS mapping to confirm the element distribution. Due to the main component of cellulose from fabric materials and polyacrylamide (pAAm) cross-linked network, carbon and oxygen were detected in the

mapping images (**Figure S3**). The nitrogen element from pAAm could also be clearly observed in **Figure S3**, forming various ionic bonds with chloropalladium anions. Here, Palladium and subsequent catalytic preparation of nickel were well distributed throughout the whole area (**Figure 2H, 2I**). Since the extremely dense aggregation of nickel nanoparticles, the most nickel content and the densest distribution were demonstrated in the mapping images, compared with other elements.

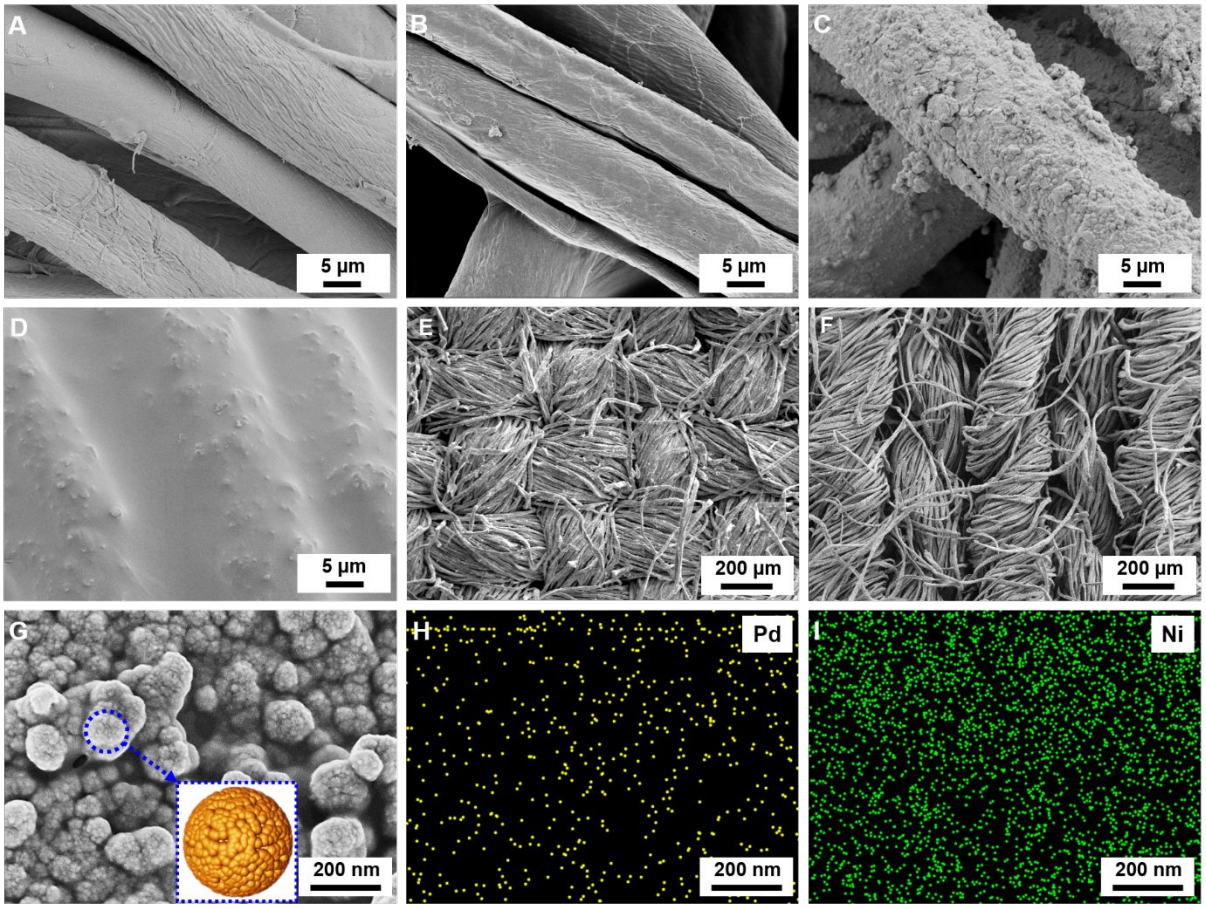

Figure 2. Representative SEM images of the as-prepared nickel-coated conductive fabrics, (A) pristine cotton fabric, (B) AAm-based fabric, (C) nickel-coated fabric *via* ELD, (D) PDMS-protected conductive fabric, (E) woven fabric (F, G) knitted fabric at low and high magnifications, respectively. The inset is the proposed microstructure of nickel nanoparticles on the fiber surface. The EDS mapping images for (H) palladium and (I) nickel.

Fourier transform infrared spectroscopy (FTIR) was further used to confirm the success of the grafting process (**Figure 3A**). The pAAm absorption peaks are located at 1660 cm^{-1} (N-H) and 1314 cm^{-1} (C-N). It is a strong proof that the pAAm has cross-linked with cellulose in the fabric. These amine groups protonated under acidic conditions and provided effective ionic

bonds with chloropalladium anions catalyst for subsequent ELD process of nickel/copper nanoparticles to realize the high conductivity of the fibers. The presence of nitrogen species was confirmed by the N 1s X-ray photoelectron spectroscopy (XPS) spectrum of the Pd-based fabric as shown in **Figure S4**. The XPS Pd 3d spectrum in **Figure 3B** displays a double feature with peaks located at 336.4 eV and 341.7 eV, which is attributed to the Pd (II) $3d_{5/2}$ and $3d_{3/2}$ signals of Pd (II) species, respectively. The Pd (II) peaks are relatively narrow and symmetrical, indicating only one chemical state of Pd (II) existing in Pd-based fabric. Then, the nickel-coated cotton fabrics and copper-coated cotton fabrics were stored for two days and characterized by X-ray diffraction (XRD) spectrum. **Figure 3C** shows that the 2θ peak at 44.9 degrees corresponds to the (111) crystal plane of nickel. **Figure 3D** demonstrates that the peaks at 43.5 and 50.6 degrees belong to the (111) and (200) crystal planes of copper, while the peak at 33.6 degrees attribute to the (111) crystal planes of copper peroxide. These results suggest that copper is easily oxidized, while nickel-coated fabric shows great air stability. For better comparison, we extracted the XRD spectrum (10-40 degrees) from **Figure 3C** (nickel-coated cotton fiber) and **Figure 3D** (copper-coated cotton fiber), as shown in **Figure S5**. According to the literature, these peaks reveal the presence of cellulose crystallite in cotton fibers.[30]

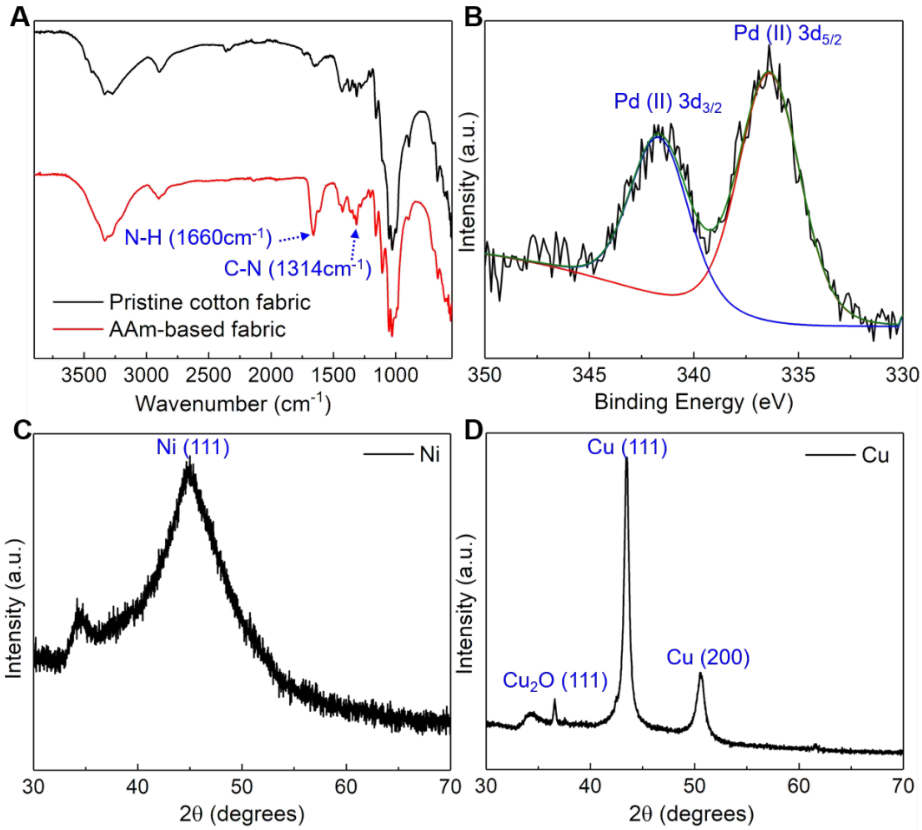

Figure 3. (A) FTIR spectrum of pristine cotton (black) and pAAm-modified cotton fabric (red). (B) The XPS Pd 3d spectrum of Pd-based fabric. XRD spectrum of (C) nickel-coated fabric and (D) copper-coated fabric stored in air for 2 days.

Moisture absorption is the main property of comfort in textiles. Cotton fabric has been attractive to people due to its outstanding absorption properties for invisible perspiration.[31, 32] To study the effect of nickel coating on the comfort performance of cotton textile, we measured the moisture regain of cotton fabric before and after nickel coating. The result indicates that the cotton after nickel coating remains 80% of its moisture absorption capacity, which is still higher than most of the synthetic fibers. Therefore, we believe that the nickel-coated cotton fabric can still maintain the comfort of raw cotton.

Although ELD technology has been developed for a long time, the metal growth mechanism *via* PAMD strategy is still unclear. Here, a series of samples at different ELD process times were measured by SEM. As shown in **Figure 1F**, catalyst-based nickel seed crystals are caged by crosslinked polymers, to upsurge the density of seed crystals on the surface of modified substrates, and to increase the conductivity in the following deposition process. The nickel seed

crystals keep growing to larger nickel particles in the ELD bath, and the final state of nickel coating on the surface of the substrate (**Figure S6**) indicates a continual film assembled from many particles. The growth process of nickel particles was shown in **Figure 4**.

Based on the classical nucleation theory,[33, 34] a thermodynamic system tends to minimize its Gibbs free energy, causing many small particles to form a spherical shape and accumulate into a circle after 5 min ELD (**Figure 4A** and **Figure S8**). According to the literature,[35] the polymers form a sparse and strong network with a mesh size on the order of 10 nm. The diameter of the initially formed nickel seed crystal is 10 nm approximately, which is consistent with the SEM result in **Figure 4A**. In this stage, the nickel particles are not continuous, and the resistance is tens of megaohms. Fast reduction induces a rapid growth of new particles in other reaction sites to form uniformly dispersed nickel seed crystals on the surface of catalyst-based cotton fabric (**Figure 4B**). Consequently, many small particles occur, and some of them break through the cage to form bigger particles after 10 min ELD and the resistance is in kilo euro level. **Figure 4C** shows an aggregation of the primary particles into a dense nickel nanoparticle film after around 20 min ELD with hundreds of ohms of resistance. Then several large nickel nanoparticles (100 nm) were grown by aggregating many small particles on the film surface (**Figure 4D**, 30 min ELD with tens of ohms of resistance) and many growth events lead to an increasing number of large particles (**Figure 4E**). Finally, all large nanoparticles aggregate into extremely dense nickel nanoparticles film with around 500 nm thickness (**Figure 4F and Figure S7**) and the final maximum resistance can reach around 3 ohms/cm.

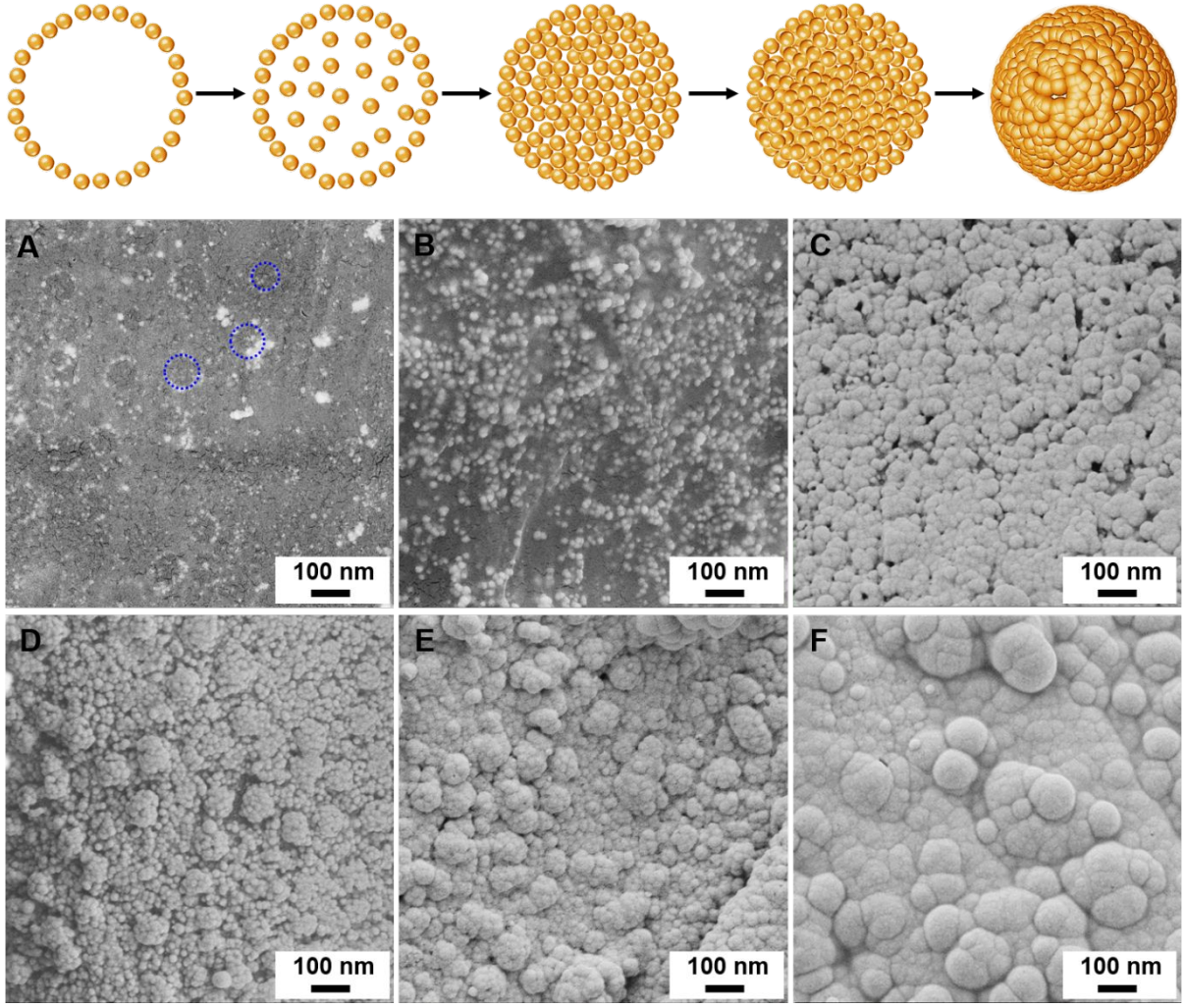

Figure 4. Representative SEM images of the nickel-coated conductive fabrics prepared at different ELD times, (A) 5 min ELD, (B) 10 min ELD, (C) 20 min ELD, (D) 30 min ELD, (E) 40 min ELD, (F) 60 min ELD.

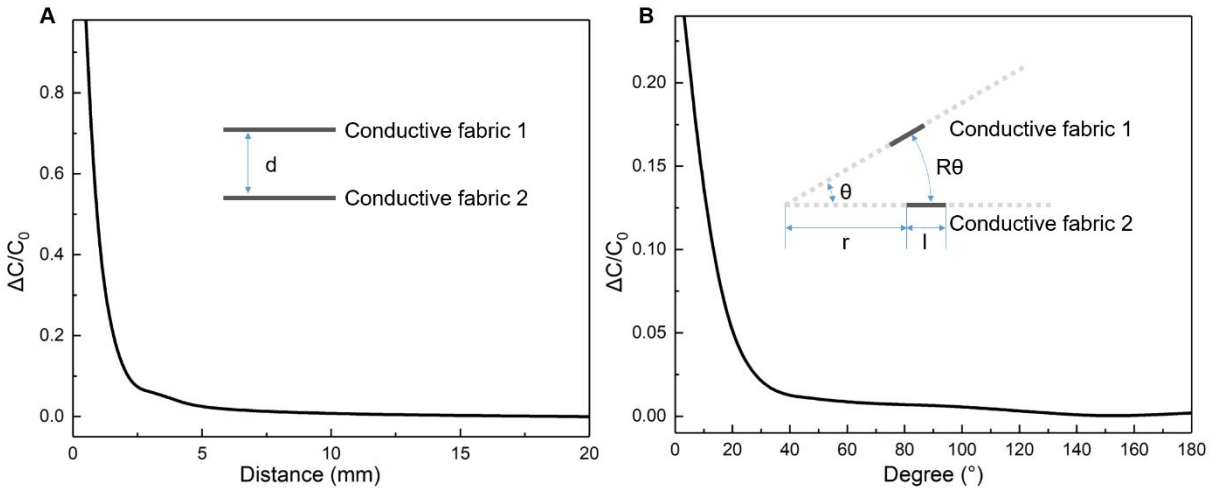

Figure 5. Capacitance change as functions of (A) distance and (B) bending angle for the conductive fabric-based sensor. The inset is the schematic diagram of parallel and non-parallel plate capacitors, respectively. Two nickel-coated fabrics with the same size were prepared. The size is 13 mm × 37 mm, and the dotted line from conductive fabric to bending center for degree test was set as 40 mm.

To understand the standalone effect of distance on the capacitive sensitivity of the proposed sensor, the relative capacitance change ($\Delta C/C_0$) was measured according to different distances (0-20 mm) between two as-prepared conductive fabrics. The ΔC and C_0 represent capacitance change and its baseline, respectively. As shown in **Figure 5A**, the capacitance is inversely proportional to the distance between the two conductive fabrics. A programmable C scan stage from Newmark systems Inc. USA, according to a previous report,[36] were operated to control the micro distance between 0-2 mm. The drive X-axis with 0.019 mm resolution controlled by an Arduino-based controller board from a host PC was used to control the distance from 0 to 20 mm, and the data interval is 0.5 mm. The electrode area (S) is constant, and as the distance between the two conductive fabrics (the inset of **Figure 5A**) monotonously decreases, the capacitance of the sensor (C) gradually increases, which is described as

$$C = \frac{\varepsilon S}{d} \quad (1)$$

where ε represents vacuum permittivity (8.85E-12 F/m), S represents the area of overlap of the two electrodes (13 mm × 37 mm) and d represents the distance between the two conductive fabrics.

To verify the reliability of the experimental result in **Figure 5A**, an analytical capacitance for different distances was carried out using equation (1). The data interval is 1E-4, so that 20 data points with the distance between 0.1 to 2 mm can be obtained. The simulations are performed *via* the MATLAB 2019a script platform. The relevant results were described in **Figure S9**, shown a similar decrease trend with the experimental result in **Figure 5A**. It demonstrated that the analytical model fitted well with the experimental results.

For Non-Parallel Plate Capacitors, the capacitance is inversely proportional to the degree of rotation angle (**Figure 5B**). The method of bending angles measurement is displayed in **Figure S10**. The relevant theoretical analysis is based on a parallel connection of capacitors.

$$\Delta V = \int \vec{E} \cdot \overrightarrow{dk} = \int_0^{\theta} E(R) R d\varphi = E(r) R\theta \quad (2)$$

Where V and E are the electric potential and electric field between two conductive fabrics; k specifies the electric field route between the two conductive fabrics; R and θ denote the relative rotating radius and angle of the integral element.

The surface charge density σ on the plates with radius of R is,

$$\sigma(R) = \varepsilon_1 \varepsilon_0 E(R) \quad (3)$$

where ε_1 is the relative permittivity of the media between the two conductive fabrics; ε_0 is the permittivity of the free space.

Combine equation (2) and (3),

$$\sigma(R) = \varepsilon_1 \varepsilon_0 \frac{\Delta V}{R\theta} \quad (4)$$

Therefore, the charge element is,

$$dq = \sigma(R) dS = \varepsilon_1 \varepsilon_0 \frac{\Delta V}{R\theta} a dR \quad (5)$$

where a is the length of the conductive fabrics.

Therefore, the integrated total charge on the capacitor is,

$$q = \frac{a\varepsilon_1 \varepsilon_0 \Delta V}{\theta} \int_r^{r+l} \frac{1}{R} dR = \frac{a\varepsilon_1 \varepsilon_0 \Delta V}{\theta} \ln\left(1 + \frac{l}{r}\right) \quad (6)$$

where r represents the radius from electrodes to the rotation center and l represents the width of the conductive fabrics.

Thus, the overall capacitance of the capacitor is,

$$C = \frac{q}{\Delta V} = \frac{a\varepsilon_1 \varepsilon_0}{\theta} \ln\left(1 + \frac{l}{r}\right) \quad (7)$$

The relevant parameters are as shown in the inset of **Figure 5B.**

By referring to the specifications of the Zurich impedance analyzer (https://www.zhinst.com/americas/products/mfia-impedance-analyzer), the minimum capacitance that the impedance analyzer can measure is 0.01 pF. By referring to capacitance signal as functions of distance and bending angle in **Figure 5**, the maximum change rate of the

capacitance deviation is 50 pF/mm and 0.2 pF/degree. Consequently, the minimum distance and bending angle deviation that can be measured are 0.2 μm and 0.05 degrees, respectively. However, due to the limitation of the accuracy of the drive X-axis of the programmable C scan stage in the practical measurement, the minimum moving distance deviation is 0.019 mm. Compared with other textile-based sensor fabrication listed in **Table S1**, the conductive textile with very low resistance was fabricated *via* an easier and cheaper strategy. The as-prepared capacitive sensor shows outstanding sensitivity and a fast response rate.

Lack of correct breathing mechanics can lead to chronic neck pain by placing abnormal loading on the front neck muscles, especially scalene, sternocleidomastoid and trapezius muscles.[37] When they become stiff and fatigued from overworking, the pain can radiate or travel into the shoulders, arms and hands. Hence, a proper breathing technique, called diaphragmatic breathing (also known as abdominal breathing), is of great significance.[38] When inhaling, the abdominal muscles relax, the diaphragm muscles contract, and the position moves down. When exhaling, the abdominal muscles contract, the diaphragm muscles relax and return to the original position. Diaphragmatic breathing brings air to the bottom portion of the chest to increase oxygenation, lowering blood pressure and relaxing muscles. In addition to reducing neck muscle strain, this breathing exercise can ensure effective ventilation of the lungs, and relieve symptoms of dyspnea. For those patients with chronic obstructive pulmonary disease (COPD) and pulmonary heart disease, the effect of such rehabilitation training can be dramatic. According to the literature,[39] fast deep breathing possibly improved respiratory muscle strength and reduced inflammatory cytokines, which is better than slow deep breathing for patients with COPD. Based on the promising results of capacitance increase with the decrease of distance in **Figure 5A**, two as-prepared nickel-coated fabrics with 13 mm × 37 mm size served as a capacitive sensor was successfully applied to monitor fast and slow deep breathing during rehabilitation training. One fabric electrode was integrated into tights and another one was fixed on the inside of a belt. When an individual inhales, the abdominal muscles relax, causing belly

out, and the distance between two conductive fabrics was reduced (**Figure 6A**), thereby generating an inhaled signal (**Figure 6B and 6C**). In reverse, when the individual exhales, the abdominal muscles contract and belly in, resulting in the distance to return to the original position to generate an exhaled signal. Here, each time interval represents a complete breathing cycle from exhalation to inspiration. **Figure 6B** shows that the person standing up slowly breathed 5 times in 27 seconds, and **Figure 6D** shows normal deep breathing of 12 times in 35 seconds. In this case, the individual standing up experiences a complete slow breathing cycle of 5.4 s, while a fast breathing cycle is 2.9 s. In the same way, the complete normal deep breathing cycle of sitting and lying is calculated as 3 s and 3.4 s, respectively (**Figure 6E and 6F**). In other words, the rate of normal diaphragmatic respiratory is the fastest when standing, the second when sitting, and the slowest when lying down. On the other hand, the relative capacitance change ($\Delta C/C_0$) of deep breathing is around 0.5 during standing, while the $\Delta C/C_0$ increase to around 1.0 and 2.0 for sitting and lying conditions respectively. Therefore, this sensor can monitor the breathing exercises in different states (standing, sitting and lying) and evaluate training intensity (slow or fast respiratory rate) to achieve different rehabilitation training effects in the same state (standing).

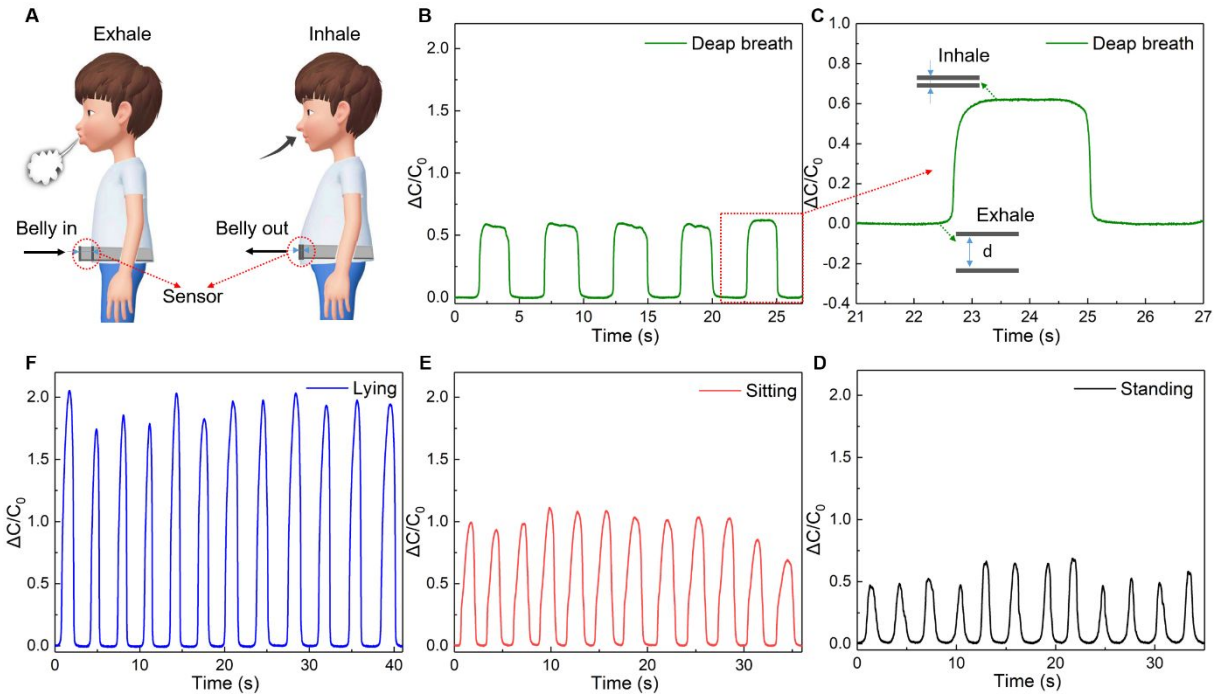

Figure 6. (A) General breathing mechanics during inhale and exhale process. Capacitance change as a function of time for distance change between two conductive fabrics affected by abdominal breathing exercise (B, C) deep breathing, and breathing activities during (D) standing, (E) sitting and (F) lying, respectively.

Monitoring of voiceprint information is a powerful strategy to help assess the pronunciation of an individual to avoid speech delay and rehabilitation training for people with language developmental delay or dysplasia. Based on the results, capacitance increase with the increase of bending angles in **Figure 5B**, the two conductive fabrics were set up on two sides of the middle throat to collect voice signal during language rehabilitation training. As shown in **Figure 7**, when a person spoke words ("Capacitance", "The University of Manchester" and "Freedom") or sentences ("Nice to meet you", "Research is my forever love" and "Thank you"), the sensor was allowed to capture the fine features of the speech by determining in real-time the change in capacitance with the movement of the vocal cords. Besides, a more significant change of capacitance was detected as the louder sound got, caused by the vibration of the vocal cords (**Figure S11**). The swallowing activity and head movement could also be monitored during rehabilitation exercise especially for head and neck cancer patients (**Figure S12 and S13**). Apart from that, another sensor (3×30 mm) was attached to the upper and lower eyelids to detect the blink speed (**Figure S14**). These results successfully imply the great performance of the textile sensor to real-time monitor fluctuation information for rehabilitation training.

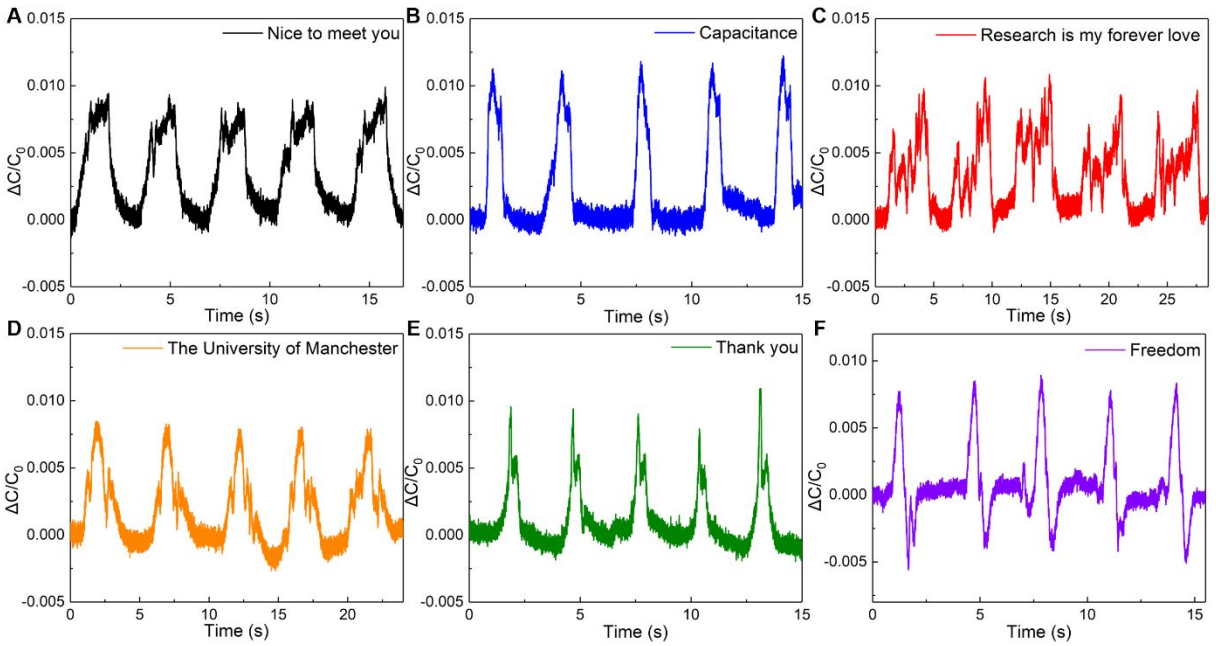

Figure 7. Capacitance fluctuation information for voiceprint recognition and correction. Repeated responses of a conductive fabric-based sensor to 6 different words (A) "Nice to meet you", (B) "Capacitance", (C) "Research is my forever love", (D) "The University of Manchester", (E) "Thank you" and (F) "Freedom".

Stability and durability are of great significance for practical applications of wearable sensors. An anthropomorphic robotic hand combining linkage-driven and tendon-driven systems was designed according to the size and geometry of a real hand, named MCR-Hand. This hand has 4 jointed fingers and 2-split palms. All joints of the MCR-Hand were driven by a built-in 18 servos to imitate all motions of a human hand (**Figure 8**). Two nickel-coated fabrics (7×16 mm) were attached to two sides of a second joint of the MCR-Hand middle finger (**Figure 8A**). The finger bending activities were repeated at a constant speed driven by a built-in servomotor and a low-level control system. The repeated bending angle is about 90 degrees. Before we collected the data in **Figure 8B**, the MCR-Hand had carried out the bending activities for more than 1 h to observe the stable output. And the bending speed was around 1 cycle/s. Some photos during the test process were taken and shown in **Figure S15**. **Figure S15** displayed the impedance-time (-300 to 0 s of the abscissa range) curve at different periods during the repeated finger bending activities monitoring. And we selected the data with around the final 3 mins, containing 2,180,000 data points to show the stable output in **Figure 8B**. As shown in **Figure 8B**, a relative

change in capacitance under repeated finger bending for hundreds of cycles exhibited high stability, durability and fast response during hundreds of cycles. The capacitance increases from around 24.3 to 26 pF during bending the middle finger joint of a human being (**Figure S16**). The capacitance changes (0.023) of the MCR-Hand is a little lower than the monitoring of finger bending activity of the real human being (0.07 in **Figure S16**), due to the smaller repeated bending angle. The selected zones are the enlarged regions of capacitance response as a function of time for anthropomorphic finger bending activities. Every measurement curve is reliably repeated well *via* the MCR-Hand built-in servo-motor control system. Besides, ordinary gloves could be worn by the robotic hand to make it match more closely to the human hand. By this way, the sensor for MCR-Hand joints motion monitoring could be assembled into normal gloves, which is user-friendly.

To further study the reliability of the sensor, we extracted three cycles of the curve from **Figure 8**, and analyzed them in detail the effect of the MCR-Hand finger bending process on the signal output (**Figure S17**). The signal output curve in every bending cycle is almost the same (very repeatable). The slight asymmetric nature, including 0.094 s, 0.13 s and 0.24 s of fluctuation, is due to the different velocity of joint motion during the MCR-Hand finger flexion/extension. The detailed explanation is as follows:

Flexion/extension of the DIP joint in the robotic finger was involved in the MAR-Hand. The DIP joint is driven by a servo motor built in the proximal phalange through a four-bar mechanism (**Figure S18**). l_1 is the driving linkage (A refers to the motor output shaft), and l_3 is the driven linkage (D refers to the joint). During the flexion of the PIP joint, the motor accelerates to a constant speed w_1 with the set acceleration a_1. When l_1 perpendicular to l_0, l_3 will reach the maximum speed, and then the speed of $l_3$will decrease. At the moment when the acceleration changes to negative from positive, there may be a short signal fluctuation. Besides, it can be seen that the four-bar mechanism structure is located on the side of the finger.

An problem with this arrangement is that when driving the DIP joint to flex, an abduction torque is simultaneously produced on the joint. When l_1 perpendicular to l_0, the pressure angle is 90 °, and the maximum input torque will appear. At the same time, the maximum abduction torque will also appear. Due to the accuracy limitations of 3D printing and structural limitations, the friction will reach the maximum value, so movement stuck phenomenon occurs. As a result, after 0.117 s accelerated movement, there was a slight fluctuation of 0.094 s in **Figure S3**. When the finger is fully extended, the extension command is still running, and it will be a delay t before entering the flexion command. During the delay time t, the motor remains energized, the finger joints keep tighten. When the delay ends, before entering to the flexion command, the motor will momentarily power off and change the direction of rotation. During the power-off period, the finger joints will relax from the tight state. And the finger joints will naturally bounce and flex, so a small peak with a slight fluctuation of 0.24 s can be observed in **Figure S3**. Similarly, a fluctuation of 0.13 s can be seen when the finger is in the final bending state.

Figure S19 provides the excellent electrical stability and durability of the conductive fabric against repeated 1500 cycles of folding and 5 cycles of washing. For folding test, the conductive fabric was folded to near 180 degrees and then unfolded back to 0 degrees. The result implied that only a little increase of the resistance (around from 3.6 to 5 Ohms) was observed after 1500 folding cycles (**Figure S19A**). We further used commercial clothing cleanser to wash the as-prepared conductive fabric for 30 min, during which the fabric was also experienced to extensive rubbing. The resistance shows a little increased around from 3.6 to 4.9 Ohms, and maintained at around 4.9 Ohms after the fourth washing cycles (**Figure S19B**). Besides, no cracks occur during folding and washing tests. The stable resistance is mainly because of the topographical interactions between coatings and substrates, as well as the protection of PDMS.

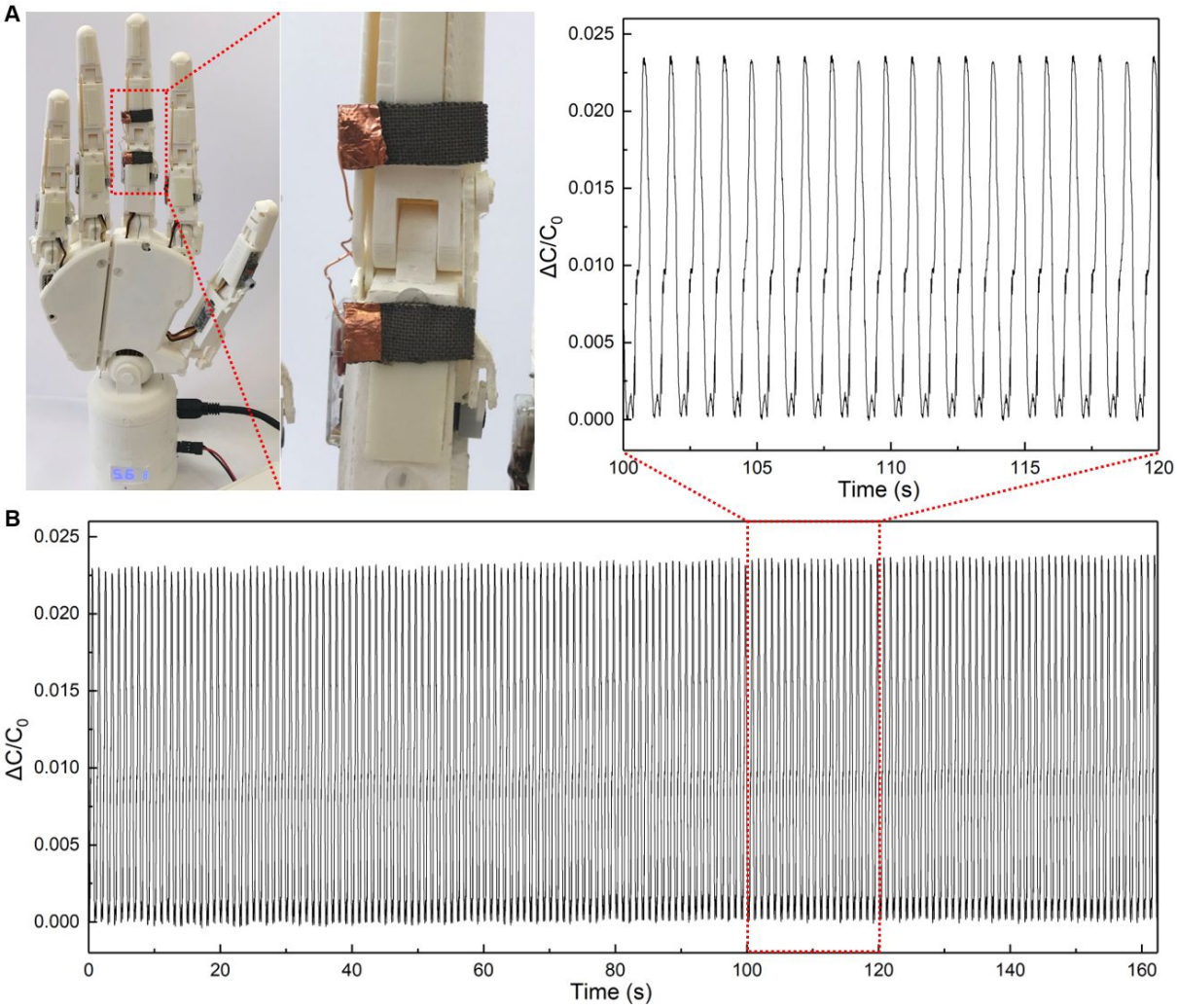

Figure 8. Relative change in capacitance under repeated finger bending of an MCR-Hand and imitating human finger bending about 90 degrees for hundreds of cycles, showing the stability and durability of the sensor.

CONCLUSION

Topological genus-3 and genus-5 structures were introduced into fiber surface modification, to improve the adhesion and conductivity of metallic coating on the fiber surface. The ammonia-containing polymer was introduced into the soft cotton fabric to form a covalent and hydrogen-bonded entangled molecular topological cage to capture catalyst-based nickel seed crystal *via* a thermally induced radical polymerization technique. The modified ELD was used for the subsequent growth of nickel nanoparticles on the surface of the catalyst-based fabric. After 10 min ELD, the seed crystal began to break through the cage to form larger particles. The continual coating around 500 nm thickness nickel nano-films could realize excellent electrical

properties of conductive fabric. The device was integrated into tights to simultaneously detect the capacitance level change with distance and angle changes between two electrodes. The monitoring results show that the sensor can be used to record dynamic information in real-time, such as breathing, speaking, blinking, head motions and joint motions in rehabilitation training. We believe this system can play a significant role in the development of high sensitivity, comfortable, durable and wearable sensors for a variety of human healthcare applications, *via* fiber surface topological modification.

EXPERIMENTAL SECTION

Materials and Instrumentation. Ammonium tetrachloropalladate(II) [$(NH_4)_2PdCl_4$], nickel sulfate hexahydrate ($NiSO_4 \cdot 6H_2O$), acrylamide (AAm) N,N'-methylene bis(acrylamide) (BIS), potassium persulfate (KPS) and all other chemicals were purchased from Sigma-Aldrich. All textile substrates were obtained from the Dye House at the University of Manchester. Scanning electron microscopy (SEM) was performed at a ZEISS Ultra-55 instrument. X-ray diffraction (XRD) data were collected using a Bruker D8 Discover (A25) theta-theta diffractometer (660 mm diameter) with a LynxEye 1D Strip detector in Bragg-Brentano geometry employing Cobalt Point/Line Focus X-ray tube with Iron kβ absorber (0.02 mm; Kβ = 1.62079 Angstrom) producing Kα radiation (Kα1 = 1.78897 Angstrom, Kα2 = 1.79285 Angstrom, Kα ratio 0.5, Kαav = 1.79026 Angstrom). Fourier transform infrared (FTIR) spectra were recorded with a Nicolet NEXUS 670 FTIR spectrometer with a liquid nitrogen cooled high-sensitivity mercury cadmium telluride (MCT) detector.

Polymer modification of cotton fabric. Firstly, cotton fabric was immersed into AAm monomer aqueous solution with 10 g/L AAm, 0.4 g/L BIS and 0.4 g/L KPS for 60°C heating for 6h. After the thermally induced radical polymerization, the poly (acrylamide) (pAAm) was chemically cross-linked with cellulose on the surface of the cotton fabric.

Palladium catalyst coated fiber/fabrics. The pAAm-based fiber/fabrics were washed with ultrapure water and hydrochloric acid (pH = 3~5) to protonate the amino groups, and immersed into an $(NH_4)_2PdCl_4$ aqueous solution (10×10^{-3} M) under dark condition for 2 h, followed by rinsing with water to remove the excess catalyst inks.

Nickel-coated fiber/fabrics. Nickel-coated fiber/fabrics preparation is an improvement on our previous reports.[20] The nickel electroless plating was performed in an ELD bath containing a 1:1 volumetric proportion of nickel-to-reductant stocks at room temperature. A nickel stock solution consisting of 20 g/L lactic acid, 40 g/L sodium citrate and 80 g/L $NiSO_4\cdot6H_2O$ was prepared in advance. A fresh reductant solution containing 10 g/L dimethylamine borane in ultrapure water was prepared separately. After mixing, the solution was adjusted with sodium hydroxide to keep the pH value at 8 to 10. The as-prepared nickel-coated fiber/fabrics were washed with water and dried in the oven for future use.

Copper-coated fiber/fabrics. The copper electroless plating was performed in an ELD bath containing a 30:1 volumetric proportion of copper-to-reductant stocks at room temperature. A copper stock solution consisting of 13 g/L sodium hydroxide, 30 g/L potassium sodium tartrate and 15 g/L copper sulfate pentahydrate was prepared in advance. 1 mL butyraldehyde was added to 30 mL copper stock solution and the mixture was left to stand for the night. Then, 10 mL fresh sodium borohydride (2 mg/L) in ice water was prepared to accelerate the copper reduction process. The as-prepared copper-coated fiber/fabrics were washed with water and dried at room temperature for future use.

Sensor Description. 3 sizes of conductive fabrics were used, (1) 13 mm × 37 mm for breathing activities, swallow and sounds monitoring, (2) 3 mm × 30 mm for blink and head movements monitoring, and (3) 7 mm × 16 mm for finger joint activity monitoring. For breathing detection, a fabric was integrated into tights and another one was fixed on the inside of a belt. For other motion detection, two conductive fabrics with the same size were integrated into different parts of the tights.

MCR-Hand Description. In this work, a robotic hand combining linkage and tendon driven system was designed according to the size and geometry of a real hand, named MCR-Hand. This hand (about 21cm) has 4 jointed fingers and 2-split palms. All joints of the MCR-Hand were driven by built-in 18 servomotors. All servos, wires and actuators were inside of the palm. Ordinary gloves could be worn by the robotic hand to make it match more closely to the human hand. So the sensor for the MCR-Hand joints, motion monitoring could be assembled into normal gloves, which is user-friendly.

Capacitance Data Acquisition. The Zurich Instruments MFIA Impedance Analyzer was used to carry out the electrical signals. A four-terminal configuration was used to interface the capacitive sensor with the impedance analyzer. The excitation frequency to carry out the capacitive measurements was fixed at 20 and 200 kHz due to its good signal-to-noise ratio (SNR). Therefore, the measurement is almost real-time since the response time is 50 and 5 us. The amplitude of voltage was fixed at 1 V. All experiments were performed at room temperature (298 K).

The relationship between the sensor impedance and its capacitance is described as

$$Z = \frac{1}{j\omega C} \tag{8}$$

where the real part of the impedance Z is probe resistance R, and imaginary part ωC represents reactance.

Generally, R can be neglected. After obtaining impedance results, real part C values are defined as

$$C = \frac{1}{\omega Z_{imag}} \tag{9}$$

For a certain constant frequency (f), part ω is a fixed parameter,

$$\omega = 2\pi f \tag{10}$$

where Z_{imag} is the impedance imaginary part of the impedance measured by the sensor connected with the Zurich Instruments MFIA Impedance Analyzer.

Therefore, different C values could be measured for the detection of human motions.

ASSOCIATED CONTENT

Supporting Information

The Supporting Information is available online at the ACS Publications website.

Schematic illustration (Figure S1, S2 and S6), EDS analysis (Figure S3), XPS N 1S spectrum (Figure S4), XRD spectrum (10-40 degrees, Figure S5), SEM images (Figure S7 and S8), Analytical capacitance change with distance (Figure S9), photos of bending angles (Figure S10), capacitance test during speech (Figure S11); swallowing (Figure S12); head movement (Figure S13); blink (Figure S14); joint bending activities (Figure S16) and MCR-Hand finger bending (Figure S15 and S17), four-bar mechanism of DIP joint (Figure S18), as well as folding and washing test (Figure S19).

AUTHOR INFORMATION

Corresponding Authors

*E-mail: xuqing.liu@manchester.ac.uk.

*E-mail: wuliang.yin@manchester.ac.uk.

ACKNOWLEDGMENTS

This research was supported by the Henry Royce Institute for Advanced Materials, funded through EPSRC grants EP/R00661X/1, EP/P025021/1, and EP/P025498/1. Wuliang Yin would thank the support from EPSRC grants EP/M020835/1. Liming Chen gratefully acknowledges the support of the President's Doctoral Scholar Award from the University of Manchester and 2018 IEEE I&M Society Graduate Fellowship Award.

REFERENCES

(1) Wang, B.; Facchetti, A. Mechanically Flexible Conductors for Stretchable and Wearable E-Skin and E-Textile Devices. *Adv. Mater.* **2019**, 1901408.

(2) Seyedin, S.; Zhang, P.; Naebe, M.; Qin, S.; Chen, J.; Wang, X.; Razal, J. M. Textile Strain Sensors: A Review of the Fabrication Technologies, Performance Evaluation and Applications. *Mater. Horiz.* **2019**, *6*, 219−249.

(3) Tessarolo, M.; Gualandi, I.; Fraboni, B. Recent Progress in Wearable Fully Textile Chemical Sensors. *Adv. Mater. Technol.* **2018**, *3*, 1700310.

(4) Heo, J. S.; Eom, J.; Kim, Y. H.; Park, S. K. Recent Progress of Textile-Based Wearable Electronics: A Comprehensive Review of Materials, Devices, and Applications. *Small* **2018**, *14*, 1703034.

(5) Slatyer, S.; Aoun, S. M.; Hill, K. D.; Walsh, D.; Whitty, D.; Toye, C. Caregivers' Experiences of a Home Support Program after the Hospital Discharge of an Older Family Member: A Qualitative Analysis. *BMC Health Serv. Res.* **2019**, *19*, 220.

(6) Baker, C. O.; Huang, X.; Nelson, W.; Kaner, R. B. Polyaniline Nanofibers: Broadening Applications for Conducting Polymers. *Chem. Soc. Rev.* **2017**, *46*, 1510−1525.

(7) Ray, T. R.; Choi, J.; Bandodkar, A. J.; Krishnan, S.; Gutruf, P.; Tian, L.; Ghaffari, R.; Rogers, J. A. Bio-Integrated Wearable Systems: A Comprehensive Review. *Chem. Rev.* **2019**, *119*, 5461−5533.

(8) Sun, F.; Tian, M.; Sun, X.; Xu, T.; Liu, X.; Zhu, S.; Zhang, X.; Qu, L. Stretchable Conductive Fibers of Ultrahigh Tensile Strain and Stable Conductance Enabled by a Worm-Shaped Graphene Microlayer. *Nano Lett.* **2019**, *19*, 6592−6599.

(9) Hu, X.; Tian, M.; Xu, T.; Sun, X.; Sun, B.; Sun, C.; Liu, X.; Zhang, X.; Qu, L. Multiscale Disordered Porous Fibers for Self-Sensing and Self-Cooling Integrated Smart Sportswear. *ACS Nano* **2020**, *14*, 559−567.

(10) Seyedin, M. Z.; Razal, J. M.; Innis, P. C.; Wallace, G. G. Strain-Responsive Polyurethane/PEDOT:PSS Elastomeric Composite Fibers with High Electrical Conductivity. *Adv. Funct. Mater.* **2014**, *24*, 2957−2966.

(11) Guo, Y.; Otley, M. T.; Li, M.; Zhang, X.; Sinha, S. K.; Treich, G. M.; Sotzing, G. A. PEDOT:PSS "Wires" Printed on Textile for Wearable Electronics. *ACS Appl. Mater. Interfaces* **2016**, *8*, 26998−27005.

(12) Lee, H. M.; Choi, S. Y.; Jung, A.; Ko, S. H. Highly Conductive Aluminum Textile and Paper for Flexible and Wearable Electronics. *Angew. Chem. Int. Ed. Engl.* **2013**, *52*, 7718−7723.

(13) Lee, J.; Kwon, H.; Seo, J.; Shin, S.; Koo, J. H.; Pang, C.; Son, S.; Kim, J. H.; Jang, Y. H.; Kim, D. E.; Lee, T. Conductive Fiber-Based Ultrasensitive Textile Pressure Sensor for Wearable Electronics. *Adv. Mater.* **2015**, *27*, 2433−2439.

(14) Chen, L.; Lu, M.; Wang, Y.; Huang, Y.; Zhu, S.; Tang, J.; Zhu, C.; Liu, X.; Yin, W. Whole System Design of a Wearable Magnetic Induction Sensor for Physical Rehabilitation. *Adv. Intell. Syst.* **2019**, *1*, 1900037.

(15) Jur, J. S.; Sweet, W. J.; Oldham, C. J.; Parsons, G. N. Atomic Layer Deposition of Conductive Coatings on Cotton, Paper, and Synthetic Fibers: Conductivity Analysis and Functional Chemical Sensing Using “All-Fiber” Capacitors. *Adv. Funct. Mater.* **2011**, *21*, 1993−2002.

(16) Selvakumar, N.; Barshilia, H. C. Review of Physical Vapor Deposited (PVD) Spectrally Selective Coatings for Mid- and High-Temperature Solar Thermal Applications. *Sol. Energy Mater. Sol. Cells* **2012**, *98*, 1−23.

(17) Loewenstein, T.; Hastall, A.; Mingebach, M.; Zimmermann, Y.; Neudeck, A.; Schlettwein, D. Textile Electrodes as Substrates for the Electrodeposition of Porous ZnO. *Phys. Chem. Chem. Phys.* **2008**, *10*, 1844−1847.

(18) Zhang, H.; Zhang, P.; Zhang, H.; Li, X.; Lei, L.; Chen, L.; Zheng, Z.; Yu, Y. Universal

Nature-Inspired and Amine-Promoted Metallization for Flexible Electronics and Supercapacitors. *ACS Appl. Mater. Interfaces* **2018**, *10*, 28963−28970.

(19) Yu, Y.; Xiao, X.; Zhang, Y.; Li, K.; Yan, C.; Wei, X.; Chen, L.; Zhen, H.; Zhou, H.; Zhang, S.; Zheng, Z. Photoreactive and Metal-Platable Copolymer Inks for High-Throughput, Room-Temperature Printing of Flexible Metal Electrodes for Thin-Film Electronics. *Adv. Mater.* **2016**, *28*, 4926−4934.

(20) Zhu, C.; Guan, X.; Wang, X.; Li, Y.; Chalmers, E.; Liu, X. Mussel-Inspired Flexible, Durable, and Conductive Fibers Manufacturing for Finger-Monitoring Sensors. *Adv. Mater. Interfaces* **2019**, *6*, 1801547.

(21) Liu, L.; Yu, Y.; Yan, C.; Li, K.; Zheng, Z. Wearable Energy-Dense and Power-Dense Supercapacitor Yarns Enabled by Scalable Graphene-Metallic Textile Composite Electrodes. *Nat. Commun.* **2015**, *6*, 7260.

(22) Li, P.; Zhang, Y.; Zheng, Z. Polymer-Assisted Metal Deposition (PAMD) for Flexible and Wearable Electronics: Principle, Materials, Printing, and Devices. *Adv. Mater.* **2019**, *31*, 1902987.

(23) Wang, X.; Yan, C.; Hu, H.; Zhou, X.; Guo, R.; Liu, X.; Xie, Z.; Huang, Z.; Zheng, Z. Aqueous and Air-Compatible Fabrication of High-Performance Conductive Textiles. *Chem. Asian J.* **2014**, *9*, 2170−2177.

(24) Liu, X.; Chang, H.; Li, Y.; Huck, W. T.; Zheng, Z. Polyelectrolyte-Bridged Metal/Cotton Hierarchical Structures for Highly Durable Conductive Yarns. *ACS Appl. Mater. Interfaces* **2010**, *2*, 529−535.

(25) Du, T.; Li, B.; Wang, X.; Yu, B.; Pei, X.; Huck, W. T.; Zhou, F. Bio-Inspired Renewable Surface-Initiated Polymerization from Permanently Embedded Initiators. *Angew. Chem. Int. Ed. Engl.* **2016**, *55*, 4260−4264.

(26) Hirzebruch, F. E. P.; Kreck, M. On the Concept of Genus in Topology and Complex Analysis. *Notices Am. Math. Soc.* **2009**, *56*, 713−719.

(27) Pandey, M.; Mohamad, N.; Amin, M. C. Bacterial Cellulose/Acrylamide pH-Sensitive Smart Hydrogel: Development, Characterization, and Toxicity Studies in ICR Mice Model. *Mol. Pharm.* **2014**, *11*, 3596−3608.

(28) Steck, J.; Yang, J.; Suo, Z. Covalent Topological Adhesion. *ACS Macro Lett.* **2019**, *8*, 754−758.

(29) Yang, J.; Bai, R.; Li, J.; Yang, C.; Yao, X.; Liu, Q.; Vlassak, J. J.; Mooney, D. J.; Suo, Z. Design Molecular Topology for Wet-Dry Adhesion. *ACS Appl. Mater. Interfaces* **2019**, *11*, 24802−24811.

(30) Cintrón, M.; Hinchliffe, D. FT-IR Examination of the Development of Secondary Cell Wall in Cotton Fibers. *Fibers* **2015**, *3*, 30−40.

(31) Bedek, G.; Salaun, F.; Martinkovska, Z.; Devaux, E.; Dupont, D. Evaluation of Thermal and Moisture Management Properties on Knitted Fabrics and Comparison with a Physiological Model in Warm Conditions. *Appl. Ergon.* **2011**, *42*, 792−800.

(32) Kadapalayam Chinnasamy, K.; Chidambaram, P. Influence of the Bamboo/Cotton Fiber Blend Proportion on the Thermal Comfort Properties of Single Jersey Knitted Fabrics. *Fibers Text. East. Eur.* **2017**, *25*, 53−57.

(33) Polte, J. Fundamental Growth Principles of Colloidal Metal Nanoparticles–A New Perspective. *CrystEngComm* **2015**, *17*, 6809−6830.

(34) Wang, J.; Mbah, C. F.; Przybilla, T.; Englisch, S.; Spiecker, E.; Engel, M.; Vogel, N. Free Energy Landscape of Colloidal Clusters in Spherical Confinement. *ACS Nano* **2019**, *13*, 9005−9015.

(35) Yang, J.; Bai, R.; Chen, B.; Suo, Z. Hydrogel Adhesion: A Supramolecular Synergy of Chemistry, Topology, and Mechanics. *Adv. Funct. Mater.* **2019**, 1901693.

(36) Xu, H.; Avila, J. R. S.; Wu, F.; Roy, M. J.; Xie, Y.; Zhou, F.; Peyton, A.; Yin, W. Imaging X70 Weld Cross-Section Using Electromagnetic Testing. *NDT E Int.* **2018**, *98*, 155−160.

(37) Celhay, I.; Cordova, R.; Miralles, R.; Meza, F.; Erices, P.; Barrientos, C.; Valenzuela, S. Effect of Upper Costal and Costo-Diaphragmatic Breathing Types on Electromyographic Activity of Respiratory Muscles. *Cranio* **2015**, *33*, 100−106.

(38) Yamaguti, W. P.; Claudino, R. C.; Neto, A. P.; Chammas, M. C.; Gomes, A. C.; Salge, J. M.; Moriya, H. T.; Cukier, A.; Carvalho, C. R. Diaphragmatic Breathing Training Program Improves Abdominal Motion During Natural Breathing in Patients with Chronic Obstructive Pulmonary Disease: A Randomized Controlled Trial. *Arch. Phys. Med. Rehabil.* **2012**, *93*, 571−577.

(39) Leelarungrayub, J.; Puntumetakul, R.; Sriboonreung, T.; Pothasak, Y.; Klaphajone, J. Preliminary Study: Comparative Effects of Lung Volume Therapy between Slow and Fast Deep-Breathing Techniques on Pulmonary Function, Respiratory Muscle Strength, Oxidative Stress, Cytokines, 6-Minute Walking Distance, and Quality of Life in Persons with COPD. *Int. J. Chron. Obstruct. Pulmon. Dis.* **2018**, *13*, 3909−3921.

ToC graphic